Probing Multiscale Factors Affecting the Reactivity of Nanoparticle-Bound Molecules

Ioulia K. Mati,[a] William Edwards,[a] Domenico Marson,[b] Edward J. Howe,[a] Scott Stinson,[a†] Paola Posocco,[b] and Euan R. Kay [a]**

[a] EaStCHEM School of Chemistry, University of St. Andrews, North Haugh, St Andrews, KY16 9ST, UK

[b] Department of Engineering and Architecture, University of Trieste, Piazzale Europa 1, 34127 Trieste (IT)

† This paper is dedicated to the memory of Scott Stinson who passed away on 20 November 2020.

ABSTRACT: The structures and physicochemical properties of surface-stabilizing molecules play a critical role in defining the properties, interactions and functionality of hybrid nanomaterials such as monolayer-stabilized nanoparticles. Concurrently, the distinct surface-bound interfacial environment imposes very specific conditions on molecular reactivity and behavior in this setting. Our ability to probe hybrid nanoscale systems experimentally remains limited, yet, understanding the consequences of surface confinement on molecular reactivity is crucial for enabling predictive nanoparticle synthon approaches for post-synthesis engineering of nanoparticle surface chemistry, and construction of devices and materials from nanoparticle components. Here, we have

undertaken an integrated experimental and computational study of the reaction kinetics for nanoparticle-bound hydrazones, which provide a prototypical platform for understanding chemical reactivity in a nanoconfined setting. Systematic variation of just one molecular-scale structural parameter – the distance between reactive site and nanoparticle surface – showed that the surface-bound reactivity is influenced by multiscale effects. Nanoparticle-bound reactions were tracked *in situ* using ^{19}F NMR spectroscopy, allowing direct comparison to the reactions of analogous substrates in bulk solution. The surface-confined reactions proceed more slowly than their solution-phase counterparts, and kinetic inhibition becomes more significant for reactive sites positioned closer to the nanoparticle surface. Molecular dynamics simulations allowed us to identify distinct supramolecular architectures and unexpected dynamic features of the surface-bound molecules that underpin the experimentally observed trends in reactivity. This study allows us to draw general conclusions regarding interlinked structural and dynamical features across several length scales that influence interfacial reactivity in monolayer-confined environments.

KEYWORDS: *self-assembled monolayers, reaction kinetics, dynamic covalent chemistry, gold nanoparticles, dissipative particle dynamics, nanoconfined chemistry, molecular dynamics*

For monolayer-stabilized nanoparticles, surface-bound molecular species play a fundamental role in tuning properties of the core material, defining interactions with the surrounding matrix, and providing a handle through which nanoparticles may be interfaced with any number of other components – be they molecular, macroscopic, or other nanomaterials.[1-6] Reliable strategies for engineering molecular-level details at the nanoparticle surface are therefore critical for realizing the technological potential of nanoparticles in any number of applications.[5, 7-10] Although chemical

functionality can be introduced into the monolayer directly during nanoparticle synthesis,[6, 11] or by 'ligand exchange' to replace sacrificial surface-bound species,[6, 11-15] post-synthesis chemical methods for modifying surface-bound species *in situ* are particularly attractive.[7-10] We have developed dynamic covalent nanoparticle building blocks as a versatile category of colloidal nanoscale synthon, which we envisage can provide generalizable chemoselective approaches for reversible and adaptive modification of nanoparticle-bound molecular functionality.[16-20] We and others have recently demonstrated that reversible covalent strategies can be used to template dynamic nanoparticle surface functionalization,[16, 21-22] to tune nanoparticle physicochemical properties,[19] to create adaptive nanoparticle assemblies,[17, 20, 23-25] and to reversibly tether nanoparticles on solid substrates.[26] For any synthetic strategy to become reliable and widely applicable, a predictive understanding of all parameters that affect reactivity must be developed. Such information will only be gradually revealed through systematic investigation of reactivity for nanoparticle-bound molecules, akin to the decades-long physical–organic understanding of bulk solution-phase reactivity that underpins molecular synthetic methods.[27]

Chemical reactivity on planar self-assembled monolayers has been the subject of numerous investigations over several decades.[28-29] However, the analytical challenge of quantifying vanishingly small concentrations of reactive species at extended surfaces with sufficient temporal resolution has proven to be a significant barrier to developing routine methods and consequently arriving at an in-depth understanding of reactivity for surface-confined species. A relatively small number of studies have revealed that reactivity can be significantly affected by surface immobilization, often resulting in kinetic behaviors that change as a reaction progresses,[30-37] and reaction rates that are influenced by several parameters, including surface roughness,[38-39] steric bulk of an incoming reactant,[11a, 11b] stereoelectronic demands of the reaction mechanism,[31]

monolayer density,[30-31, 40] and, for mixed-ligand monolayers, the molecular structures and mole fractions of reactive and non-reactive components.[32-34, 36, 41-43]

Monolayer-stabilized nanoparticles – which can be formulated as homogenous solutions or colloidal suspensions – offer a rare platform on which the behavior of surface-confined molecules can be investigated using ensemble analytical techniques capable of probing molecular-level structural details. Yet, for these nanoscale hybrid constructs there are several factors that may affect reactivity: from the size and shape distribution defining the population in each sample, to the heterogeneity of binding sites around any one nanoparticle; the influence of the underlying nanoparticle surface curvature on packing of the surface-bound species, to the potential for inter-monolayer interactions between molecules on different nanoparticles. A number of investigators have sought to understand the thermodynamics of simple equilibria and dynamic binding events (particularly involving biomolecules) on nanoscale surfaces,[44-77] but very few studies have probed the kinetic consequences of surface confinement. The seminal work of Murray and co-workers examined product distributions to establish that, in contrast to the solution-phase reaction, nucleophilic substitution of nanoparticle-bound alkylbromides by primary amines yielded exclusively secondary amine products.[78] Furthermore, shielding of the surface-bound reactive sites by longer unreactive ligands significantly retarded reaction progress and enhanced the influence of nucleophile steric demand on the nanoparticle-bound reaction.[78] Workentin and co-workers have noted significantly reduced reactivity for nanoparticle-bound maleimides in Diels–Alder cycloadditions,[79] and for methyl-2-(diphenylphosphino)benzoate-terminated monolayers in the Staudinger–Bertozzi ligation with azides;[80] the latter being ascribed to inter-particle clustering of the starting nanoparticles. On the other hand, the same researchers observed no significant

difference between bulk solution and nanoparticle-bound kinetics for the strain-promoted cycloaddition of acetylenes, at least for a low surface density of reactive groups.[81]

Clearly, a large and complex parameter space controls reactivity for nanoparticle-bound molecules. This presents a significant fundamental physical–organic challenge if surface-confined reactions are to be applied routinely for manipulating and assembling chemically reactive nanoparticle components. The high level of constitutional detail now available experimentally in turn informs accurate simulation of the nanoparticle-bound environment. Modelling can provide crucial insights that plug the gaps in experimentally accessible information, yet has not been applied to understanding covalent reactivity. Here we describe a combined experimental and computational study which begins to unravel this multi-parameter challenge for hydrazone-based dynamic covalent nanoparticles.[16, 19-20] Specifically, we set out to isolate the effect of monolayer depth on the reaction kinetics for a hydrazone at the monolayer periphery by preparing a self-consistent series of monolayer-stabilized gold nanoparticles (AuNPs). We were able to track reactions in real time using *in situ* ^{19}F NMR, thereby establishing reaction profiles from which kinetic parameters could be extracted. Simulations of the nanoparticle-bound molecular monolayers in turn uncovered several parameters – on the molecular, supramolecular and nanoscale levels – that influence reactivity, even for this ostensibly simple reaction system.

Results and Discussion

Nanoparticle-confined hydrazone hydrolysis. With the aim of isolating the effect of just one parameter – monolayer depth – on nanoparticle-bound hydrazone reactivity, we designed nanoparticle-stabilizing ligands C_y-**1**H (Chart 1), in which an *N*-acylhydrazone reactive site is linked to a thiol surface anchor group by an alkyl chain of variable length (y carbon atoms).

Fluorobenzylidine hydrazones were employed so as to exploit the simplicity, sensitivity and wide chemical shift dispersity of ^{19}F NMR spectra for *in situ* reaction monitoring.[16, 19-20] In order to produce a self-consistent nanoparticle series, ligands C_y-**1**H were installed on gold cores by ligand exchange from hexanethiyl-stabilized nanoparticle precursors. Rigorous purification from all non-surface-bound species was achieved by repeated cycles of nanoparticle precipitation, washing, and re-suspension, followed by purity assessment by ^{1}H, ^{19}F{^{1}H} and T_2-filtered ^{1}H NMR spectroscopy. Imaging by transmission electron microscopy (TEM) before and after ligand exchange indicated only minimal changes to the nanoparticle size distribution during this process. Nanoparticle solutions in a mixture of 10% D_2O/THF (*v*/*v*) were colloidally stable at sufficiently high concentrations of hydrazones ([AuNP-C_y-**1**] ≈ 4 mM) to allow real-time non-destructive reaction monitoring by ^{19}F{^{1}H} NMR spectroscopy. Concentrations of all fluorinated species were thereby quantified by signal area deconvolution relative to an internal standard of known concentration. Structurally analogous model compound **2** was also prepared to allow comparison of nanoparticle-bound reactivity with reaction in bulk solution.

Chart 1. Molecular structures of hydrazone-terminated alkanethiol ligands C_y-**1**H, model compound **2** and hydrazone-functionalized nanoparticles AuNP-C_y-**1**.

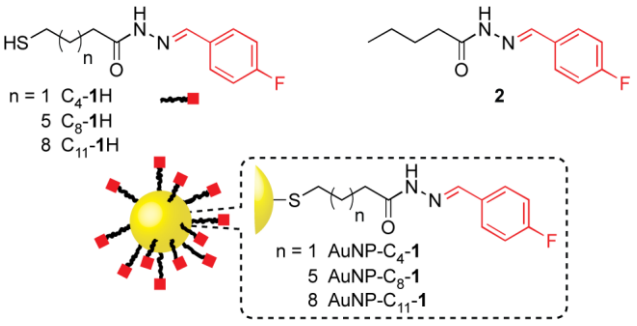

Nanoparticles such as AuNP-C_y-**1** where the nucleophilic hydrazide unit is anchored to the monolayer are modified by dynamic covalent exchange of the electrophilic benzylidine unit with

an alternative carbonyl component.[16] In the absence of excess nucleophile, a direct transamination pathway[82-83] is not expected to be kinetically significant. Rather, attack by water leading to hydrazone hydrolysis is the key kinetic step for post-synthetic modifications of 'nucleophilic' dynamic covalent nanoparticles of this sort.[20] We investigated the rate of acid-catalyzed hydrolysis for nanoparticle-bound and bulk solution hydrazones AuNP-C_y-**1** and **2**, respectively. Under the standard conditions, the extent of hydrolysis for model compound **2** reached only ca. 12%, consistent with the high hydrolytic stability of typical *N*-acylbenzylidine hydrazones.[82] Generating only low concentrations of hydrazide gave us confidence that the nanoparticle-bound reactions could be studied in the absence of confounding effects such as nanoparticle cross-linking, or unforeseen kinetic pathways that might become significant at high concentrations of surface-bound hydrazides.

In-line with our experience with similar but structurally more complicated systems,[16, 20] the rate of the nanoparticle-bound reactions was found to be slower than the reaction in bulk solution, although the extent of inhibition is relatively modest. The reaction profiles were satisfactorily fitted by a reversible kinetic model that is pseudo-first order in the hydrolysis direction (rate constant k_{hydr}) and second order in the condensation direction (rate constant k_{cond}) (Figures 1, S10 and Tables 1, S1–S4). Comparison of k_{cond} to the apparent second-order rate constant for hydrolysis ($k_{app–hydr}$) reveals that the hydrolysis process is approximately 5 orders of magnitude slower than condensation, confirming that hydrolysis is the kinetically significant step during exchange of the electrophilic benzylidine unit. A clear trend was observed in the rate constant for the hydrolysis reaction with monolayer depth (k_{hydr}, Figure 1, Table 1): the reaction becoming increasingly slower as the hydrazone reactive site is moved closer to the nanoparticle surface (inhibition factors relative to bulk solution of ×0.6, ×0.4, ×0.2 for C_{11}, C_8, C_4 methylene chains respectively).

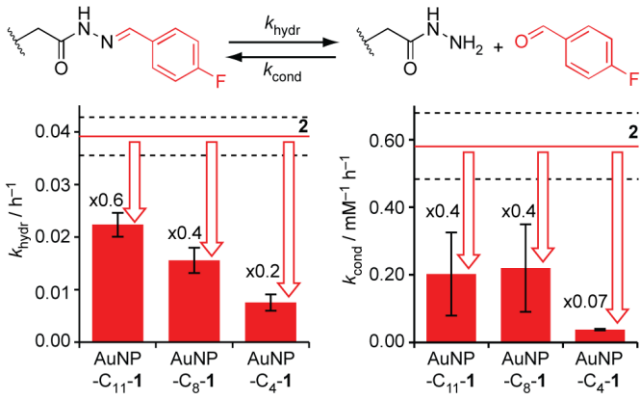

Figure 1. Pseudo-first-order rate constants (k_{hydr}) and second-order rate constants (k_{cond}) for the forward and reverse reaction, respectively, under hydrazone hydrolysis conditions for nanoparticle-bound reactions (bars) compared to reaction in bulk solution (horizontal line). Surface-inhibition factors (= *k*(NP) / *k*(bulk solution)) are given for each nanoparticle-bound reaction. Error bars (dotted lines for reaction of **2**) represent one standard deviation from the mean of triplicate measurements or better. Rate constants for all individual replicates can be found in the Supporting Information. Conditions: [AuNP-C$_y$-**1**]$_0$ or [**2**]$_0$ ≈ 4 mM, [CF_3CO_2H] = 20 mM, D_2O/THF (1:9 *v*/*v*), 294 K.

Table 1. Kinetic data for hydrazone hydrolysis.[a]

substrate	k_{hydr} / 10^{-3} h^{-1}	$k_{app-hydr}$ / mM^{-1} h^{-1}	k_{cond} / mM^{-1} h^{-1}	*K* / mM
2	39 ± 5	7.0×10^{-6}	0.6 ± 0.1	0.07
AuNP-C$_{11}$-**1**	22 ± 2	4.0×10^{-6}	0.2 ± 0.1	0.1
AuNP-C$_8$-**1**	16 ± 2	2.8×10^{-6}	0.2 ± 0.1	0.07
AuNP-C$_4$-**1**	8 ± 2	1.4×10^{-6}	0.037 ± 0.002	0.2

[a] Values are given as mean ± one standard deviation for triplicate measurements or better. Apparent second-order rate constants for hydrolysis ($k_{app-hyrd}$) calculated from the observed pseudo-first-order rate constant (k_{hydr}) assuming a water concentration of 5530 mM. Conditions: [AuNP-C$_y$-**1**]$_0$ or [**2**]$_0$ ≈ 4 mM, D_2O/THF (1:9 *v*/*v*), [CF_3CO_2H] = 20 mM, 294 K. Kinetic data for each replicate are given in Tables S1–S4.

In contrast to the consistent values measured for k_{hydr}, no clear trend was observed for the condensation rate constant (k_{cond}, Figure 1, Table 1). In fact, significant variability in the value of k_{cond} was observed between replicates. In most experiments, the condensation process was retarded more strongly than the hydrolysis step, corresponding to a reaction endpoint that favors more hydrolysis on the nanoparticle surface compared to bulk solution. However, the extent of this effect was quite different across individual repeats. For AuNP-C_{11}-**1** and AuNP-C_8-**1**, at least one replicate yielded an anomalously small value of k_{cond}, corresponding to a reaction profile that did not reach equilibrium within the timescale of the experiment (25 h). Only AuNP-C_4-**1** exhibited a consistent behavior, with every experiment showing continued reaction well beyond the expected equilibrium endpoint based on the reactivity in bulk solution. The experiments exhibiting very slow condensation rates also tend to produce larger fitting uncertainties for the k_{cond} parameter, suggesting that the simple kinetic model is not properly describing the reaction progress in these cases.

Preparing further batches of each nanoparticle gratifyingly confirmed the same conclusions regarding k_{hydr} values, but failed to produce a more consistent picture for the condensation rate – in fact revealing the same significant variability in k_{cond} values for AuNP-C_4-**1** as had been observed for the other monolayer depths in the earlier experiments (Figure S11, Tables S1–S4). Several features demanded consideration as the source of this variability. The molecular-level structural integrity of the ligand shell on each nanoparticle batch was examined by oxidative desorption using iodine, allowing analysis of all previously surface-bound species in bulk solution (Figure S9). These experiments verified that each hydrazone was present and structurally intact. However, in each case, a small proportion (6–24%) of residual hexanethiyl ligands was also detected. Additionally, there were minor variations in nanoparticle core size for substrates not

prepared from the same starting nanoparticle batch (for sample details for each experiment, see Tables S2–S4). Yet, neither the proportion of unreactive ligand, nor nanoparticle core size, could be correlated with the variation in k_{cond}. We therefore ascribe the slower values observed in a subset of replicates to stochastic processes that occur as the reaction proceeds, such as nucleation-driven aggregation or surface binding of released hydrazides at defects in the monolayer.

Simplifying the picture: Nanoparticle-confined hydrazone exchange. In order to circumvent unanticipated reaction pathways that become kinetically significant as increasing concentrations of surface-bound hydrazides are exposed, we further simplified the system by performing hydrazone exchange in the presence of a large excess of 4-nitrobenzaldehyde (**3**, 50 equivalents). Under these 'trapping' conditions AuNP-C_y-**1** are converted quantitatively into AuNP-C_y-**4**, *via* a two-step hydrolysis–condensation mechanism (Figure 2). The kinetic model can therefore be reduced to an irreversible process defined by a pseudo-first-order rate constant k_{trap}.[16, 20] We furthermore endeavored to maintain consistency across all experiments by scaling up our synthetic procedures to ensure that all repeats could be performed from single batches of nanoparticles with similar size distributions ($\langle d \rangle$ = 3.8–4.2 nm) and proportions of residual hexanethiyl ligand (12–14%). Taking these precautions led to very reproducible quantitative results (Figure 2). All four reaction systems (AuNP-C_y-**1** for y = 4, 8, 11 and model compound **2**) exhibited a first-order reaction profile (Figure S12), from which k_{trap} was extracted by nonlinear fitting (Tables 2, S5–S8).

Noting that under hydrolysis conditions the apparent second-order rate constants for hydrolysis ($k_{app\text{-}hydr}$, Table 1) are approximately 5 orders of magnitude smaller than the observed rates for condensation (k_{cond}), we expected the hydrolysis step for exchange to be rate determining. Indeed, under trapping conditions no intermediate free hydrazide was observed in any experiment, and the

pseudo-first-order rate constants k_{trap} (Table 2) are similar in magnitude to the pseudo-first-order rate constant for hydrolysis k_{hydr} (Table 1), confirming that these conditions probe the kinetically significant step for hydrazone exchange on 'nucleophilic' dynamic covalent nanoparticles.[16, 20] Pleasingly, k_{trap} also exhibits a very similar dependency on the monolayer depth to that observed for k_{hydr}: once again, the nanoparticle-bound reaction is slower compared to the same process in bulk solution, with more significant inhibition observed the closer the reactive site is to the surface (inhibition factors of ×0.4, ×0.3, ×0.1 for C_{11}, C_8, C_4 alkyl chain lengths respectively, Figure 2).

Examining the absolute values of the rate constants reveals further subtle details. In bulk solution, the value of k_{trap} is slightly larger than k_{hydr}, likely as a result of the increased solvent polarity when high concentrations of 4-nitorbenzaldehyde (ca. 0.2 M) are introduced (a further small increase in rate was observed for trapping experiments carried out in the presence of 100 molar equivalents 4-nitrobenzaldehyde). Conversely, for the nanoparticle-bound reactions, the values of k_{trap} are almost identical to those for k_{hydr}, suggesting that the monolayer environment is less susceptible to changes in properties of the bulk matrix.

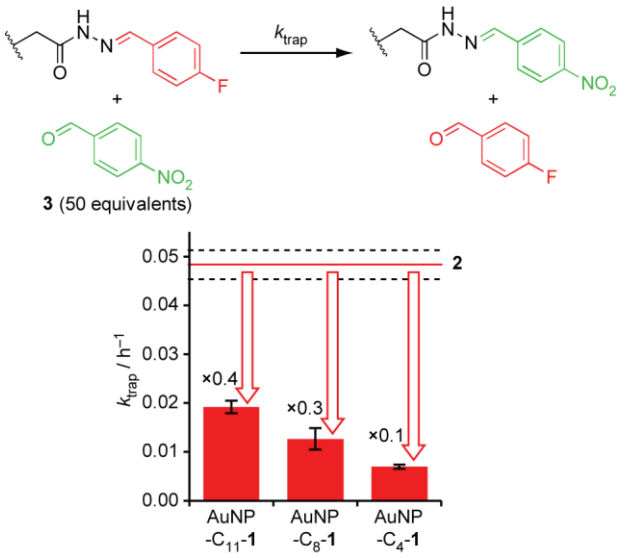

Figure 2. Pseudo-first-order rate constants (k_{trap}) for exhaustive hydrazone exchange in the presence of an excess of 4-nitrobenzaldehyde, 3, for nanoparticle-bound reactions (bars) compared to reaction of model compound **2** in bulk solution (horizontal line). Surface-inhibition factors are given for each nanoparticle-bound reaction. Error bars (dotted lines for reaction of **2**) represent one standard deviation from the mean of triplicate measurements or better. Rate constants for individual replicates can be found in the Supporting Information, Tables S5–S8. Conditions: [AuNP-C$_y$-**1**]$_0$ or [**2**]$_0$ ≈ 4 mM, [**3**]$_0$ = 0.2 M, [CF_3CO_2H] = 20 mM, D_2O/THF (1:9 *v*/*v*), 294 K.

Table 2. Pseudo-first-order rate constants k_{trap} for hydrazone exchange in the presence of excess 4-nitrobenzaldehyde.[a]

substrate	k_{trap} / ×10^{-3} h^{-1}
2	48 ± 3
AuNP-C$_{11}$-**1**	19 ± 1
AuNP-C$_8$-**1**	13 ± 2
AuNP-C$_4$-**1**	7.0 ± 0.4

[a] Values are given as mean ± one standard deviation for triplicate measurements or better. Conditions: [AuNP-C_y-**1**]$_0$ or [**2**]$_0$ ≈ 4 mM, [**3**]$_0$ = 0.2 M, [CF_3CO_2H] = 20 mM, D_2O/THF (1:9 *v*/*v*), 294 K. Kinetic data for each replicate are given in Tables S5–S8.

The trapping experiments revealed one further unanticipated observation. In reactions of AuNP-C_{11}-**1**, it was observed that the starting concentrations of nanoparticle-bound hydrazones measured by quantitative $^{19}F\{^1H\}$ NMR spectroscopy were consistently lower than the final concentration of 4-fluorobenzaldehyde released by the end of the experiment. This was contrary to our previous experience with similar systems,[16, 20] and the same phenomenon was not observed for either AuNP-C_8-**1** nor AuNP-C_4-**1**. For AuNP-C_8-**1**, good agreement was always observed between the concentration of starting hydrazone estimated by quantitative $^{19}F\{^1H\}$ NMR spectroscopy on the surface-bound species before addition of the acid catalyst, and the concentration of released 4-fluorobenzaldehyde at the end of the reaction. The significantly slower reaction of AuNP-C_4-**1** meant that the reaction did not reach completion within the experiment timescale (25 h), however the starting hydrazone concentration was verified by comparing quantitative $^{19}F\{^1H\}$ NMR spectroscopy measurement of the surface-bound species, with measurement of the surface-released species in bulk solution following oxidative ligand desorption (Figure S14). For analyzing the reactions of AuNP-C_{11}-**1**, correcting the starting hydrazone concentration based on the concentration of 4-fluorobenzaldehyde released under exhaustive exchange conditions significantly improved the goodness of fit when estimating the pseudo-first-order rate constant.

These observations led us to consider whether the concentration discrepancy for AuNP-C_{11}-**1** could be a result of colloidally stable aggregates, for which the ^{19}F NMR resonances of surface-bound hydrazones may be significantly broadened to the extent that a proportion of the signal is lost in the spectral baseline noise. The mean solvodynamic diameters measured by dynamic light scattering (DLS) in 10% H_2O/THF for all three samples (AuNP-C_4-**1**: 7.6 ± 0.4 nm, AuNP-C_8-**1**:

9.8 ± 0.4 nm, AuNP-C_{11}-**1**: 9.7 ± 2.2 nm, Table S9) were in good agreement with the expected values based on the known dimensions of the core and molecular monolayer and with the results of nanoparticle modelling discussed in the following section. Only at higher solvent polarities were colloidally stable aggregates observed (Figure S15). In order to probe for aggregation at higher concentrations representative of those used for studying reaction kinetics, diffusion ordered (DOSY) NMR spectroscopy experiments were performed to establish a diffusion coefficient for each nanoparticle at ca. 4 mM concentration (in terms of surface-bound ligand) in 10% D_2O/THF. These values were then used to estimate the hydrodynamic size (see Supporting Information, Section 6). Using this method, the hydrodynamic diameter for AuNP-C_4-**1** was estimated to be 7.6 nm, in excellent agreement with the known nanoparticle dimensions and the results from DLS (Table S9). DOSY NMR analysis of AuNP-C_8-**1** and AuNP-C_{11}-**1** gave solvodynamic sizes (11.2 nm and 15.4 nm respectively) that are, only to a very small extent, larger than the expected dimensions. These results therefore suggest that all three nanoparticle samples are relatively well dispersed in 10% H_2O/THF. However, the greater than expected increases in size with alkyl chain length observed by DOSY analysis may indicate formation of small aggregates, perhaps in equilibrium with well-dispersed nanoparticles, for systems stabilized by longer alkyl chain monolayers at higher concentrations. Noncovalent nanoparticle aggregation might conceivably be yet another factor that influences reaction kinetics. Nevertheless, AuNP-C_{11}-**1** still exhibit the fastest reaction kinetics. It would be instructive to design future studies that deconvolute the effect of hierarchical nanoparticle interactions on reaction kinetics for surface bound molecules.

Molecular modelling of the nanoparticle-confined reaction environment. The kinetic significance of the hydrolysis process suggests that surface-confined reactivity and the experimentally observed trends in reaction rate according to differences in ligand structure can be

understood through their influence on the rate-determining nucleophilic attack of water at the nanoparticle-bound hydrazone. Molecular models of the nanoparticle-bound monolayer morphology (Figure 3) revealed distinct differences in the ligand-shell packing, dependent on the length of alkyl chain spacer. The shortest C_4 ligands adopt an overall disordered monolayer morphology. Thus, the incoming water nucleophile must diffuse between ligands to reach the reactive hydrazone site. Attack at the benzylidine carbon along the reactive Bürgi–Dunitz trajectory will correspondingly be significantly hindered. By inspecting the average water distribution close to the benzylidine carbon for AuNP-C_4-**1** (Figure 4a), we see that the density of water molecules is significantly decreased with respect to bulk as an effect of local solvent confinement induced by the monolayer. At the other extreme, the C_{11} ligands adopt a 'bundled' structure, driven by favorable van der Waals interactions between the longer methylene chains and π–π stacking of the aromatic headgroups. In this arrangement, a high proportion of the reactive sites (on average 54% of C_{11} ligands, Figure 5a) are solvent-exposed and water nucleophiles can more readily attack at the benzylidine carbon along the reactive trajectory. Indeed, the water density distribution for AuNP-C_{11}-**1** (Figure 4c) shows that the concentration of water molecules at bundle interfaces (here bundles correspond to red areas) is close to, but still lower than, the bulk value. It is important to note that the experimental evidence indicated no effect of ligand length on reaction endpoint, and that the hydrolysis kinetics for AuNP-C_{11}-**1** exhibit a normal first-order behavior. Thus, ligand bundling does not appear to result in two populations of ligands with differing reactivity. Surface confinement significantly restricts molecular conformational flexibility and this effect is felt more strongly by ligands in the bundle interiors compared to solvent-exposed ligands. This can be seen by comparing the ensemble average standard deviation of individual chain end-to-end distance, $\langle\sigma_{ee}\rangle$, for ligands in the solvent-exposed and bundle

interior surface environments with the same molecules in bulk solution (Figure 5b). Larger values of $\langle\sigma_{ee}\rangle$ indicate chains that can fluctuate more over time (see Computation Studies section for the definition of $\langle\sigma_{ee}\rangle$). Likewise, the standard deviation of the individual chain standard deviations of end-to-end distance, $\langle\sigma_{\sigma}\rangle$, quantifies the heterogeneity in chain motions for the different surface-confined environments (Figure 5c). Across all nanoparticle-bound environments, the outer ligands in AuNP-C_{11}-**1** are the most exposed to water-rich solvent, have the highest conformational mobility and greatest diversity of motions available, all of which increase the chance of a water–hydrazone encounter along the reactive trajectory. Nonetheless, the significant surface-associated kinetic inhibition is explained by the fact that almost half the ligands on Au-C_{11}-**1** are shielded from the solvent – reducing the effective concentration of the reaction substrate – while even ligands on the bundle peripheries are significantly less conformationally mobile than in bulk solution (Figure 5b) – reducing the probability of a reactive water–substrate encounter. As the reaction progresses, increased conformational freedom allows inner ligands to become solvent accessible, explaining the absence of two distinct ligand populations. By contrast, the disordered ligand shell of AuNP-C_4-**1** is characterized by uniformly low conformational mobility and poor penetration by the water-rich solvent, with a correspondingly even lower probability of water–hydrazone encounters along the reactive trajectory, and hence, slower reaction kinetics.

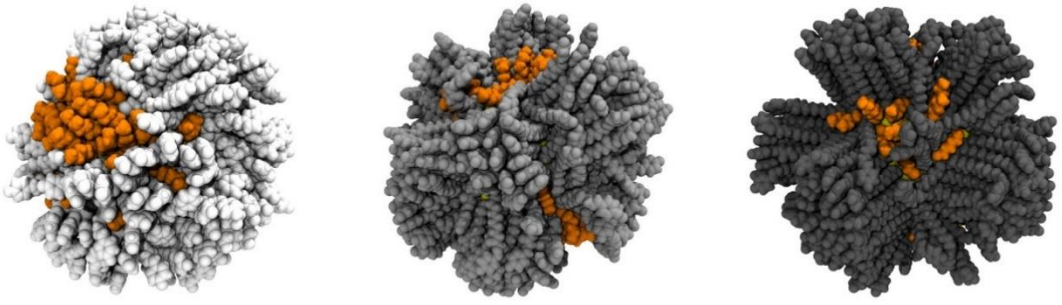

AuNP-C_4-**1** AuNP-C_8-**1** AuNP-C_{11}-**1**

Figure 3. The effect of alkyl spacer length on ligand monolayer morphology determined by atomistic simulation for AuNP-C_y-**1**. For the longest alkyl spacer (AuNP-C_{11}-**1**) a bundled ligand shell is formed, resulting in a high proportion of reactive sites easily accessible to attack from external nucleophiles. The shortest spacer (AuNP-C_4-**1**) exhibits a disordered ligand shell, which hinders attack of external nucleophiles along the appropriate reactive trajectories, and the intermediate ligand length (AuNP-C_8-**1**) likewise exhibits an intermediate semi-ordered ligand monolayer. In orange are depicted the unreactive hexanethiyl ligands that remain after ligand exchange.

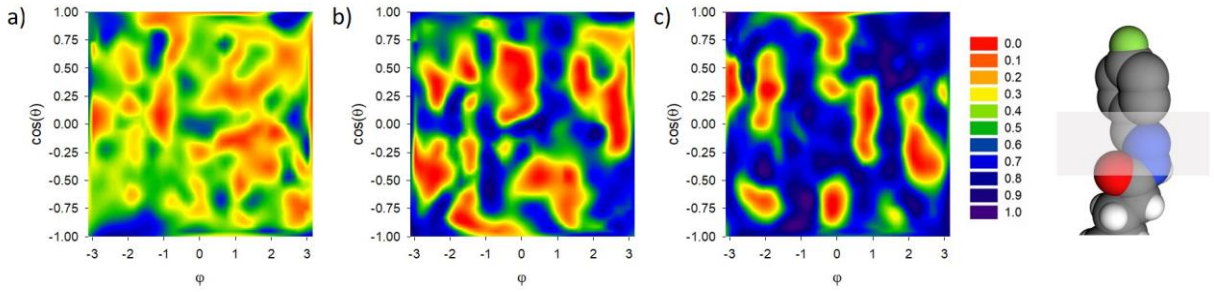

Figure 4. Averaged normalized water density distribution calculated on spherical surfaces close to the benzylidine carbon for AuNP-C_4-**1** (a), AuNP-C_8-**1** (b), and AuNP-C_{11}-**1** (c). The plots show the distribution as a two-dimensional projection of the sphere surface (x-axis, the azimuthal angle φ; y-axis, the cosine of the polar angle θ). Values are normalized to water density in bulk solvent.

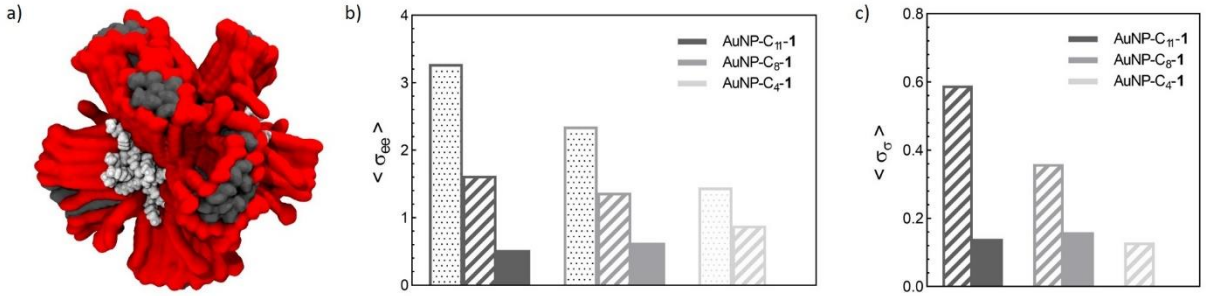

Figure 5. (a) Snapshot of AuNP-C_{11}-**1** highlighting C_{11} solvent-exposed ligands in red. Residual hexanethiyl ligands are displayed in white. (b) and (c) Ensemble average of the time-series standard deviation of the individual chain end-to-end distance $<\sigma_{ee}>$ and standard deviation of the individual chain standard deviations of the chain end-to-end distance $<\sigma_{\sigma}>$ for solvent-exposed (hatched bars), inner (filled bars) and isolated bulk (dotted bars) ligands. For AuNP-C_4-**1**, values are averaged over all chains as no bundles are formed.

Our detailed experimental constitutional characterization of the three nanoparticles (Figures S1–S9) evidenced the presence of residual hexanethiyl ligands after ligand exchange, which were included in the molecular models. Mesoscale calculations revealed that these short chains form small isolated patches within the monolayer (see Figure 3 and Figure S17). Length mismatch and difference in bulkiness are known to promote microphase separation of mixtures of ligands through maximization of the conformational entropy gained by forming extended interfaces.[5, 84-87] Nonetheless, for these systems this has a limited influence on the overall monolayer organization (*e.g.* bundled *vs.* isotropic, see Figure S18) likely due to the low proportion of hexanethiyl ligands (12–14%). Only in AuNP-C_{11}-**1** and AuNP-C_8-**1** the presence of the additional interfaces endows more ligands with a higher configurational mobility, which leads to slightly higher values of $<\sigma_{ee}>$ for solvent-exposed chains (compare Figure S19a,b with Figure 5b,c). The protonation state of nanoparticle-bound hydrazones can be expected to influence the monolayer morphology and ligand dynamics. Although we were unable to experimentally measure directly the fraction of protonated hydrazones under the experimental conditions, measurements on model compounds in bulk solution allowed us to estimate 5 mol% as an upper limit for the fraction of protonated ligands. Nanoparticles including this fixed number of charged ligands in the simulation showed no qualitative differences in monolayer structure, solvation or ligand dynamics (compare Figures

S20–S22 with Figures 3–5). We therefore concluded that our molecular models can be considered appropriate for rationalizing the experimental results under the current experimental conditions.

Combining experimental and computational insights to complete the picture of nanoparticle-confined reactivity. This systematic experimental and computational study aimed to isolate the effect of only one structural feature, yet has revealed several factors affecting reaction rate of nanoparticle-bound molecules that do not exist for analogous reactions taking place in bulk solution. The effects of surface confinement on reaction kinetics can be rationalized as resulting from the specific microenvironment at the interfacial reaction site, the influence of the surrounding matrix on meeting the stereoelectronic demands of the reaction mechanism, and the effect of noncovalent interactions between reaction sites and neighboring surface-confined species (or species on other nanoparticles that are in close proximity). Together, the structure of the nanoparticle core and the chemical constitution of the surface-stabilizing monolayer define the multiscale structural and dynamic features of the surface-bound reaction environment, representing a much wider and relationally complex parameter space than for conventional physical–organic analysis of reactions in bulk solution.

Kinetic inhibition of reactions in the sterically crowded surface-bound setting compared to bulk solution was intuitively expected. Successful reaction requires nucleophilic attack at the benzylidine carbon atom along appropriate trajectories. Although the relatively diffuse π^* orbitals, symmetrically distributed either side of the planar benzylidine unit, remain reasonably accessible to incoming nucleophiles for some hydrazones,[31] ligand bundling decreases the effective concentration of solvent-exposed 'reactive' substrates. In comparison to bulk solution, the interfacial environment and reduced conformational mobility lower the probability of reactive encounters. Surface inhibitions of several orders of magnitude – or even complete inhibition –

have been observed for mechanistically similar reactions at the termini of self-assembled monolayers on planar substrates.[36-37, 40, 88] Ascribed to large negative entropies of activation on account of steric crowding at the monolayer periphery,[89-91] the largest inhibitions occur for monolayers with a high density of reactive sites and low numbers of defects.[32-33, 36, 39-40, 88] Our observation of only modest inhibition exemplifies a fundamental difference between planar-surface and nanoparticle-bound monolayers, in that the latter are intrinsically defect rich. Our molecular dynamics simulations illustrate that disorder can be manifested through either formation of small locally ordered ligand bundles, leaving a large proportion of mobile solvent-exposed exterior ligands, or else entirely disordered ligand shell morphologies, which can correspond to less-reactive substrates.

Increasing kinetic inhibition as the reactive site is moved closer to the nanoparticle surface is a surface-specific effect that has no analogue for reactions in bulk solution. Perhaps counter-intuitively, it is the disordered monolayer formed by the shortest ligand that leads to the most significant kinetic inhibition. This is in direct contrast to 2D self-assembled monolayers, where less-ordered packing on account of weaker inter-chain dispersion interactions leads to increased reaction rates.[36] Our simulations confirm that shorter alkyl spacers produce less-ordered monolayers, but also reveal that this morphology results in restricted conformational mobility and hindered penetration of the water nucleophile towards the reactive site. On curved nanoparticle substrates, the increasingly favorable intermolecular interactions between longer alkyl chains can only be accommodated by formation of closely packed bundles to give a spatially heterogeneous ligand shell. The anisotropic ligand organization results in interfaces where ligands are readily accessible to incoming water molecules. Moreover, molecules at bundle interfaces experience fewer favorable ligand–ligand interactions, so that they are highly conformationally dynamic.

Altogether, this results in faster reaction rates for the bundled monolayers formed by longer ligands. As the reaction proceeds, the significant conformational mobility of ligands on the bundle 'exteriors' allows inner ligands to be attacked by the nucleophile, so that the bundled monolayers on AuNP-C_8-**1** and AuNP-C_{11}-**1** react significantly faster than the disordered ligand shell on AuNP-C_4-**1**.

This study aimed to isolate just one molecular-level structural parameter but revealed effects on both structure and dynamics across several length-scales that in-turn influence reactivity. There are several other distinctive traits of the nanoparticle-bound environment that will likewise require dedicated study to determine their impact on reactivity. The hydrophobic interfacial environment, which requires desolvation of incoming nucleophiles, might play a role in retarding reaction kinetics. It is interesting to note that, even for neutral water nucleophiles attacking electrophilic sites at the monolayer periphery, the trapping experiments suggest that the nanoparticle-bound reaction is less susceptible to differences in solvent polarity than the reaction in bulk solution. Finally, we cannot rule out the possibility that noncovalent interactions between neighboring ligands might influence the reactivity of nanoparticle-bound hydrazones through changes to pK_a values,[69] or otherwise affecting the stability of key intermediates.[83, 92]

Even if a small proportion of AuNP-C_{11}-**1** are present as transient aggregates, this was nevertheless the fastest reacting nanoparticle substrate, suggesting that aggregation does not play a significant role under the conditions investigated here. Furthermore, the hydrolysis and exchange reactions of all three nanoparticle systems were well-described by simple kinetic models. This was corroborated by excellent agreement between the initial rate of reaction (k_{init}) in each case and the pseudo-first-order rate constants estimated over the full reaction time course (Tables S6, S7, S8), indicating that there is no significant change in kinetic behavior – and therefore no kinetically

important changes to aggregation state – as the reactions proceed. Under trapping conditions, the lack of kinetic dependency on reaction extent is consistent with the sterically isomorphous nature of the exchanging aldehyde units. Conversely, despite hydrazone hydrolysis proceeding to only modest conversions in the bulk-solution setting, significant variability in the extent of reaction was observed for the nanoparticle-bound scenario, which could not be correlated with structural features. These considerations serve as a reminder that intrinsically inhomogeneous nanoscale reaction substrates are susceptible to subtle effects of population diversity and to stochastic or defect-initiated events, posing unavoidable challenges to predicting ensemble chemical behavior.

Conclusion

In contrast to the indirect *ex situ*, surface-specific or single-molecule analytical methods that have been required to probe reactivity at planar surfaces,[28-29, 93-94] the 'pseudomolecular' nature of well-defined monolayer-stabilized nanoparticles provides a readily accessible platform on which to study surface-bound reactivity at the ensemble level. The ability to track real-time concentrations of surface-bound and bulk-solution species simultaneously, using non-destructive analytical methods, allows the established approaches of physical–organic chemistry to be applied to nanoscale surface-confined systems, and consequently, comparisons made to directly analogous solution-phase reactions. A self-consistent series of gold nanoparticles stabilized by alkylthiyl monolayers differing only in one molecular parameter has allowed us to systematically study how molecular-level structure affects surface-bound reactivity, leading to conclusions that extend beyond the specific systems under investigation. Ostensibly small changes to molecular structure affect reactivity through interlinked factors on several length scales, including the consequences of mesoscale monolayer ordering on local microenvironment and ligand conformational mobility. It can be expected that both of these factors similarly influence any number of reactions involving

attack of an external nucleophile at surface-confined reactive sites. Such surface-specific traits have no parallel in bulk solution-phase settings, and established structure–reactivity trends for extended 2D monolayers should also not be relied upon to predict the behavior of defect-rich highly curved nanoparticle-stabilizing monolayers. Distinct from both small-molecule studies in bulk solution and highly uniform 2D monolayers, structural heterogeneity and susceptibility to stochastic events are inescapable intrinsic characteristics of nanoscale reaction substrates, posing a significant challenge to predictive understanding of chemical behavior. Nevertheless, detailed experimental constitutional characterization facilitates accurate computational modelling of the nanoparticle-bound monolayer at both mesoscale and atomic levels, granting insight on structural and dynamical features that are not revealed by experimental methods alone. Far from opening a Pandora's box of interconnected parameters that we may not wish to have to consider, developing a complete understanding of this complex picture is an exciting experimental and computational challenge at the intersection of physical–organic chemistry, supramolecular chemistry, nanochemistry and surface science. This endeavor will be critical if we aspire to reach the same level of predictive structure–reactivity understanding of chemical behavior and reactivity across a range of emerging nanoconfined systems[95] as we currently have for small-molecules in solution.

METHODS

Nanoparticle synthesis and structural characterization. Detailed synthetic procedures and characterization data for all organic molecules and nanoparticles can be found in the Supporting Information. Hydrazone-functionalized gold nanoparticles were prepared by ligand exchange from hexanethiyl-stabilized precursor nanoparticles, followed by purification by multiple rounds of precipitation, centrifugation, decanting and resuspension, as previously described.[19] Purity from

all unbound molecular contaminants was determined by ^{1}H and $^{19}F\{1H\}$ NMR spectroscopy (Figures S3, S6).

Size distributions for each batch of nanoparticles (Figures S1, S4, S7) were determined by deposition of one drop of nanoparticle suspension on holey carbon films supported on a 300 mesh Cu grid, followed by imaging using a JEM 2011 TEM. Image analysis was carried out using the software *ImageJ*.

The molecular composition of each monolayer was determined quantitatively by oxidative ligand desorption. A solution of AuNP in $CDCl_3$ or THF-d_8 (chosen depending on the known solubility of each hydrazone ligand) was prepared, and to which a small quantity of iodine was added. Quantitative ^{1}H NMR spectra (relaxation delay time: 30 s) were acquired at several time intervals until no further change was observed. The sharp signals for all desorbed species could be assigned by reference to authentic samples (*e.g.* Figure S9). Relative concentrations were established by area deconvolution of appropriate signals.

Thermogravimetic analysis (Figures S2, S5, S8) was used to determine the organic content of the sample. The density of the nanoparticle-stabilizing monolayers was then estimated by assuming isotropic gold cores of size equal to the mean size determined by TEM, and an effective molecular weight for surface-bound ligands determined from oxidative ligand desorption.

Determination of reaction kinetics. Reactions were performed in THF/D_2O (9:1 *v*/*v*) at a starting hydrazone concentration of ca. 4.0 mM in the presence of CF_3CO_2H (20 mM) and internal standard 4-fluorotoluene (4.0 mM). Stock solutions of 4-fluorotoluene and CF_3CO_2H were prepared volumetrically. Concentrations of all fluorine-containing species were monitored by quantitative $^{19}F\{^{1}H\}$ NMR against the known concentration of internal standard. A solution of AuNP-C_y-**1** (or model compound **2**) was prepared in THF/D_2O to which was added an aliquot of

4-fluorotoluene. The concentration of hydrazone **1** (or **2**) was determined by NMR against the known concentration of internal standard. The reaction was started by addition of an aliquot of CF_3CO_2H stock to give a final concentration of 20 mM. The sample was kept at a room temperature (measured as 21 °C) and reaction progress monitored at various time intervals over 24 h. A pseudo-first-order hydrolysis rate constant (k_{hydr}) and second-order condensation rate constant (k_{cond}) were estimated by nonlinear fitting of the experimental data using the software package COPASI. Representative kinetic profiles are shown in Figure S10 and the results for each experimental replicate can be found in Tables S1–S4.

Reaction kinetics under irreversible exhaustive exchange conditions were determined in a similar manner with the addition of 50 equivalents (with respect to starting hydrazone) of 4-nitrobenzaldehyde. In this case, the data was fitted to an irreversible kinetic model to give a single pseudo-first-order rate constant (k_{trap}). Representative kinetic profiles are shown in Figure S12 and the results for each experimental replicate can be found in Tables S5–S8.

Computational Studies. The self-organization of each AuNP-C_y-**1** monolayer was first retrieved at coarse-grained level by dissipative particle dynamics calculations following a computational procedure developed by the group and already successfully used to study several chemically different ligand combinations on gold nanoparticles.[84-87] These nanoparticle structures were then mapped back to all-atom configurations to gain molecular-level details. The monolayers were equilibrated in explicit THF/water solvent mixture at room temperature for solvent analysis and structural characterization. Coarse-grained simulations were carried out in LAMMPS,[96-97] while atomistic calculations were performed using AMBER 18.[98] Details on the parameterization and simulations can be found in the Supporting Information.

Average of standard deviation of individual chain end-to-end distance, $<\sigma_{ee}>$, is calculated as $\langle\sigma_{ee}(i)\rangle_E$, where $\sigma_{ee}(i)$ is the mean standard deviation (over simulation time) of the individual chain i end-to-end distance and $\langle \quad \rangle_E$ denotes ensemble average over all ligand chains. Standard deviation of the individual chain standard deviation of end-to-end distance, $<\sigma_\sigma>$, is derived as $[\langle\sigma_{ee}(i)^2\rangle_E - \langle\sigma_{ee}(i)\rangle_E^2]^{1/2}$.[99]

ASSOCIATED CONTENT

Supporting Information. General experimental procedures; detailed synthetic methods and structural characterization for all compounds and nanoparticles; detailed experimental procedures for determination of reaction kinetics; results for all experimental replicates; determination of nanoparticle aggregation state by DOSY NMR and DLS; computational methods and additional computational results. This material is available free of charge *via* the Internet at http://pubs.acs.org.

AUTHOR INFORMATION

Corresponding Author

*paola.posocco@dia.units.it

*ek28@st-andrews.ac.uk

NOTES

The authors declare no competing financial interest. The research data underpinning this publication can be accessed at: https://doi.org/10.17630/0c05bebb-30d0-4705-9551-7b71269a6e00 [Reference 100].

ACKNOWLEDGMENT

We thank Dr Tomas Lebl and Dr Siobhan Smith for assistance running and analyzing DOSY NMR experiments, Mr Ross Blackley for assistance with TEM imaging, and Prof. Garry Taylor for access to dynamic light scattering instrumentation. Mass spectrometry was carried out at the EPSRC UK National Mass Spectrometry Facility (NMSF) at Swansea University, at the University of St Andrews.

I. K. M., W. E., E. J. H, S. S. and E. R. K. are grateful for funding from the Leverhulme Trust [RPG-2015-042], the Engineering and Physical Sciences Research Council [EP/K016342/1], the University of St Andrews, and the EPSRC Centre for Doctoral Training in Critical Resource Catalysis (CRITICAT) [Ph.D. studentship to SS: EP/L016419/1]. D. M. and P.P thank the Italian Ministry of University Research (MIUR) for funding [RBSI14PBC6].

REFERENCES

(1) Moyano, D. F.; Rotello, V. M. Nano Meets Biology: Structure and Function at the Nanoparticle Interface. *Langmuir* **2011**, *27*, 10376-10385.

(2) Shaw, C. P.; Fernig, D. G.; Lévy, R. Gold Nanoparticles as Advanced Building Blocks for Nanoscale Self-Assembled Systems. *J. Mater. Chem.* **2011**, *21*, 12181-12187.

(3) Xu, L.; Ma, W.; Wang, L.; Xu, C.; Kuang, H.; Kotov, N. A. Nanoparticle Assemblies: Dimensional Transformation of Nanomaterials and Scalability. *Chem. Soc. Rev.* **2013**, *42*, 3114-3126.

(4) Boles, M. A.; Ling, D.; Hyeon, T.; Talapin, D. V. The Surface Science of Nanocrystals. *Nature Mater.* **2016**, *15*, 141-153.

(5) Pengo, P.; Sologan, M.; Pasquato, L.; Guida, F.; Pacor, S.; Tossi, A.; Stellacci, F.; Marson, D.; Boccardo, S.; Pricl, S.; Posocco, P. Gold Nanoparticles with Patterned Surface Monolayers for Nanomedicine: Current Perspectives. *Eur. Biophys. J.* **2017**, *46*, 749-771.

(6) Heuer-Jungemann, A.; Feliu, N.; Bakaimi, I.; Hamaly, M.; Alkilany, A.; Chakraborty, I.; Masood, A.; Casula, M. F.; Kostopoulou, A.; Oh, E.; Susumu, K.; Stewart, M. H.; Medintz, I. L.; Stratakis, E.; Parak, W. J.; Kanaras, A. G. The Role of Ligands in the Chemical Synthesis and Applications of Inorganic Nanoparticles. *Chem. Rev.* **2019**, *119*, 4819-4880.

(7) Sperling, R. A.; Parak, W. J. Surface Modification, Functionalization and Bioconjugation of Colloidal Inorganic Nanoparticles. *Philos. Trans. R. Soc. A* **2010**, *368*, 1333-1383.

(8) Sapsford, K. E.; Algar, W. R.; Berti, L.; Gemmill, K. B.; Casey, B. J.; Oh, E.; Stewart, M. H.; Medintz, I. L. Functionalizing Nanoparticles with Biological Molecules: Developing Chemistries That Facilitate Nanotechnology. *Chem. Rev.* **2013**, *113*, 1904-2074.

(9) Edwards, W.; Kay, E. R. Manipulating the Monolayer: Responsive and Reversible Control of Colloidal Inorganic Nanoparticle Properties. *ChemNanoMat* **2016**, *2*, 87-98.

(10) Biju, V. Chemical Modifications and Bioconjugate Reactions of Nanomaterials for Sensing, Imaging, Drug Delivery and Therapy. *Chem. Soc. Rev.* **2014**, *43*, 744-764.

(11) Hühn, J.; Carrillo-Carrion, C.; Soliman, M. G.; Pfeiffer, C.; Valdeperez, D.; Masood, A.; Chakraborty, I.; Zhu, L.; Gallego, M.; Yue, Z.; Carril, M.; Feliu, N.; Escudero, A.; Alkilany, A. M.; Pelaz, B.; del Pino, P.; Parak, W. J. Selected Standard Protocols for the Synthesis, Phase Transfer, and Characterization of Inorganic Colloidal Nanoparticles. *Chem. Mater.* **2017**, *29*, 399-461.

(12) Hostetler, M. J.; Green, S. J.; Stokes, J. J.; Murray, R. W. Monolayers in Three Dimensions: Synthesis and Electrochemistry of Omega-Functionalized Alkanethiolate-Stabilized Gold Cluster Compounds. *J. Am. Chem. Soc.* **1996**, *118*, 4212-4213.

(13) Ingram, R. S.; Hostetler, M. J.; Murray, R. W. Poly-Hetero-Omega-Functionalized Alkanethiolate-Stabilized Gold Cluster Compounds. *J. Am. Chem. Soc.* **1997**, *119*, 9175-9178.

(14) Kassam, A.; Bremner, G.; Clark, B.; Ulibarri, G.; Lennox, R. B. Place Exchange Reactions of Alkyl Thiols on Gold Nanoparticles. *J. Am. Chem. Soc.* **2006**, *128*, 3476-3477.

(15) Caragheorgheopol, A.; Chechik, V. Mechanistic Aspects of Ligand Exchange in Au Nanoparticles. *Phys. Chem. Chem. Phys.* **2008**, *10*, 5029-5041.

(16) della Sala, F.; Kay, E. R. Reversible Control of Nanoparticle Functionalization and Physicochemical Properties by Dynamic Covalent Exchange. *Angew. Chem. Int. Ed.* **2015**, *54*, 4187-4191.

(17) Borsley, S.; Kay, E. R. Dynamic Covalent Assembly and Disassembly of Nanoparticle Aggregates. *Chem. Commun.* **2016**, *52*, 9117-9120.

(18) Kay, E. R. Dynamic Covalent Nanoparticle Building Blocks. *Chem. - Eur. J.* **2016**, *22*, 10706-10716.

(19) Edwards, W.; Marro, N.; Turner, G.; Kay, E. R. Continuum Tuning of Nanoparticle Interfacial Properties by Dynamic Covalent Exchange. *Chem. Sci.* **2018**, *9*, 125-133.

(20) Marro, N.; della Sala, F.; Kay, E. R. Programmable Dynamic Covalent Nanoparticle Building Blocks with Complementary Reactivity. *Chem. Sci.* **2020**, *11*, 372-383.

(21) Nowak, P.; Saggiomo, V.; Salehian, F.; Colomb-Delsuc, M.; Han, Y.; Otto, S. Localized Template-Driven Functionalization of Nanoparticles by Dynamic Combinatorial Chemistry. *Angew. Chem. Int. Ed.* **2015**, *54*, 4192-4197.

(22) Han, Y.; Nowak, P.; Colomb-Delsuc, M.; Leal, M. P.; Otto, S. Instructable Nanoparticles Using Dynamic Combinatorial Chemistry. *Langmuir* **2015**, *31*, 12658-12663.

(23) Mikšátko, J.; Aurélio, D.; Kovaříček, P.; Michlová, M.; Veverka, M.; Fridrichová, M.; Matulková, I.; Žáček, M.; Kalbáč, M.; Vejpravová, J. Thermoreversible Magnetic Nanochains. *Nanoscale* **2019**, *11*, 16773-16780.

(24) Wang, Y.; Santos, P. J.; Kubiak, J. M.; Guo, X.; Lee, M. S.; Macfarlane, R. J. Multistimuli Responsive Nanocomposite Tectons for Pathway Dependent Self-Assembly and Acceleration of Covalent Bond Formation. *J. Am. Chem. Soc.* **2019**, *141*, 13234-13243.

(25) Zentner, C. A.; Concellón, A.; Swager, T. M. Controlled Movement of Complex Double Emulsions *via* Interfacially Confined Magnetic Nanoparticles. *ACS Cent. Sci.* **2020**, *6*, 1460-1466.

(26) Kovaříček, P.; Cebecauer, M.; Neburková, J.; Bartoň, J.; Fridrichová, M.; Drogowska, K. A.; Cigler, P.; Lehn, J.-M.; Kalbac, M. Proton-Gradient-Driven Oriented Motion of Nanodiamonds Grafted to Graphene by Dynamic Covalent Bonds. *ACS Nano* **2018**, *12*, 7141-7147.

(27) Whitesides, G. M. Physical-Organic Chemistry: A Swiss Army Knife. *Isr. J. Chem.* **2016**, *56*, 66-82.

(28) Chechik, V.; Crooks, R. M.; Stirling, C. J. M. Reactions and Reactivity in Self-Assembled Monolayers. *Adv. Mater.* **2000**, *12*, 1161-1171.

(29) Sullivan, T. P.; Huck, W. T. S. Reactions on Monolayers: Organic Synthesis in Two Dimensions. *Eur. J. Org. Chem.* **2003**, 17-29.

(30) Koloski, T. S.; Dulcey, C. S.; Haralson, Q. J.; Calvert, J. M. Nucleophilic Displacement Reactions at Benzyl Halide Self-Assembled Monolayer Film Surfaces. *Langmuir* **1994**, *10*, 3122-3133.

(31) Fryxell, G. E.; Rieke, P. C.; Wood, L. L.; Engelhard, M. H.; Williford, R. E.; Graff, G. L.; Campbell, A. A.; Wiacek, R. J.; Lee, L.; Halverson, A. Nucleophilic Displacements in Mixed Self-Assembled Monolayers. *Langmuir* **1996**, *12*, 5064-5075.

(32) VanRyswyk, H.; Turtle, E. D.; Watson-Clark, R.; Tanzer, T. A.; Herman, T. K.; Chong, P. Y.; Waller, P. J.; Taurog, A. L.; Wagner, C. E. Reactivity of Ester Linkages and Pentaammineruthenium(III) at the Monolayer Assembly/Solution Interface. *Langmuir* **1996**, *12*, 6143-6150.

(33) Schonherr, H.; Chechik, V.; Stirling, C. J. M.; Vancso, G. J. Monitoring Surface Reactions at an AFM Tip: An Approach to Follow Reaction Kinetics in Self-Assembled Monolayers on the Nanometer Scale. *J. Am. Chem. Soc.* **2000**, *122*, 3679-3687.

(34) Kwon, Y.; Mrksich, M. Dependence of the Rate of an Interfacial Diels-Alder Reaction on the Steric Environment of the Immobilized Dienophile: An Example of Enthalpy-Entropy Compensation. *J. Am. Chem. Soc.* **2002**, *124*, 806-812.

(35) Banks, J. T.; Yu, T. T.; Yu, H. Z. Direct Visualization of the Hydrolysis Kinetics of Titanium(IV) Alkoxides on Functionalized Gold Surfaces. *J. Phys. Chem. B* **2002**, *106*, 3538-3542.

(36) Dordi, B.; Schonherr, H.; Vancso, G. J. Reactivity in the Confinement of Self-Assembled Monolayers: Chain Length Effects on the Hydrolysis of *N*-Hydroxysuccinimide Ester Disulfides on Gold. *Langmuir* **2003**, *19*, 5780-5786.

(37) Luo, Y.; Bernien, M.; Krueger, A.; Hermanns, C. F.; Miguel, J.; Chang, Y. M.; Jaekel, S.; Kuch, W.; Haag, R. *In Situ* Hydrolysis of Imine Derivatives on Au(111) for the Formation of Aromatic Mixed Self-Assembled Monolayers: Multitechnique Analysis of This Tunable Surface Modification. *Langmuir* **2012**, *28*, 358-366.

(38) Neogi, P.; Neogi, S.; Stirling, C. J. M. Reactivity of Carboxy Esters in Gold Thiol Monolayers. *J. Chem. Soc., Chem. Commun.* **1993**, 10.1039/c39930001134, 1134-1136.

(39) Rajalingam, K.; Bashir, A.; Badin, M.; Schroder, F.; Hardman, N.; Strunskus, T.; Fischer, R. A.; Woll, C. Chemistry in Confined Geometries: Reactions at an Organic Surface. *ChemPhysChem* **2007**, *8*, 657-660.

(40) Vaidya, B.; Chen, J. H.; Porter, M. D.; Angelici, R. J. Effects of Packing and Orientation on the Hydrolysis of Ester Monolayers on Gold. *Langmuir* **2001**, *17*, 6569-6576.

(41) Chechik, V.; Stirling, C. J. M. Reactivity in Self-Assembled Monolayers: Effect of the Distance from the Reaction Center to the Monolayer-Solution Interface. *Langmuir* **1998**, *14*, 99-105.

(42) Yousaf, M. N.; Chan, E. W. L.; Mrksich, M. The Kinetic Order of an Interfacial Diels-Alder Reaction Depends on the Environment of the Immobilized Dienophile. *Angew. Chem. Int. Ed.* **2000**, *39*, 1943-1946.

(43) Liu, Y. J.; Navasero, N. M.; Yu, H. Z. Structure and Reactivity of Mixed Co-Carboxyalkyl/Alkyl Monolayers on Silicon: ATR-FTIR Spectroscopy and Contact Angle Titration. *Langmuir* **2004**, *20*, 4039-4050.

(44) Daniel, M. C.; Ruiz, J.; Nlate, S.; Blais, J. C.; Astruc, D. Nanoscopic Assemblies between Supramolecular Redox Active Metallodendrons and Gold Nanoparticles: Synthesis, Characterization, and Selective Recognition of H_2PO^{4-}, HSO^{4-}, and Adenosine-5'-Triphosphate (ATP^{2-}) Anions. *J. Am. Chem. Soc.* **2003**, *125*, 2617-2628.

(45) Astruc, D.; Daniel, M.-C.; Ruiz, J. Dendrimers and Gold Nanoparticles as Exo-Receptors Sensing Biologically Important Anions. *Chem. Commun.* **2004**, 2637-2649.

(46) You, C. C.; De, M.; Han, G.; Rotello, V. M. Tunable Inhibition and Denaturation of Alpha-Chymotrypsin with Amino Acid-Functionalized Gold Nanoparticles. *J. Am. Chem. Soc.* **2005**, *127*, 12873-12881.

(47) You, C. C.; De, M.; Rotello, V. M. Mono Layer-Protected Nanoparticle-Protein Interactions. *Curr. Opin. Chem. Biol.* **2005**, *9*, 639-646.

(48) Verma, A.; Rotello, V. M. Surface Recognition of Biomacromolecules Using Nanoparticle Receptors. *Chem. Commun.* **2005**, 10.1039/b410889b, 303-312.

(49) De, M.; You, C. C.; Srivastava, S.; Rotello, V. M. Biomimetic Interactions of Proteins with Functionalized Nanoparticies: A Thermodynamic Study. *J. Am. Chem. Soc.* **2007**, *129*, 10747-10753.

(50) You, C. C.; Agasti, S. S.; Rotello, V. M. Isomeric Control of Protein Recognition with Amino Acid- and Dipeptide-Functionalized Gold Nanoparticles. *Chem. - Eur. J.* **2008**, *14*, 143-150.

(51) Phillips, R. L.; Miranda, O. R.; Mortenson, D. E.; Subramani, C.; Rotello, V. M.; Bunz, U. H. F. Gold Nanoparticle-PPE Constructs as Biomolecular Material Mimics: Understanding the Electrostatic and Hydrophobic Interactions. *Soft Matter* **2009**, *5*, 607-612.

(52) Yeh, Y.-C.; Rana, S.; Mout, R.; Yan, B.; Alfonso, F. S.; Rotello, V. M. Supramolecular Tailoring of Protein-Nanoparticle Interactions Using Cucurbituril Mediators. *Chem. Commun.* **2014**, *50*, 5565-5568.

(53) Chen, K. M.; Rana, S.; Moyano, D. F.; Xu, Y. S.; Guo, X. H.; Rotello, V. M. Optimizing the Selective Recognition of Protein Isoforms through Tuning of Nanoparticle Hydrophobicity. *Nanoscale* **2014**, *6*, 6492-6495.

(54) Manea, F.; Houillon, F. B.; Pasquato, L.; Scrimin, P. Nanozymes: Gold-Nanoparticle-Based Transphosphorylation Catalysts. *Angew. Chem. Int. Ed.* **2004**, *43*, 6165-6169.

(55) Lucarini, M.; Franchi, P.; Pedulli, G. F.; Pengo, P.; Scrimin, P.; Pasquato, L. EPR Study of Dialkyl Nitroxides as Probes to Investigate the Exchange of Solutes between the Ligand Shell of Monolayers of Protected Gold Nanoparticles and Aqueous Solutions. *J. Am. Chem. Soc.* **2004**, *126*, 9326-9329.

(56) Lucarini, M.; Franchi, P.; Pedulli, G. F.; Gentilini, C.; Polizzi, S.; Pengo, P.; Scrimin, P.; Pasquato, L. Effect of Core Size on the Partition of Organic Solutes in the Monolayer of Water-Soluble Nanoparticles: An ESR Investigation. *J. Am. Chem. Soc.* **2005**, *127*, 16384-16385.

(57) Perrone, B.; Springhetti, S.; Ramadori, F.; Rastrelli, F.; Mancin, F. "NMR Chemosensing" Using Monolayer-Protected Nanoparticles as Receptors. *J. Am. Chem. Soc.* **2013**, *135*, 11768-11771.

(58) Salvia, M. V.; Rarnadori, F.; Springhetti, S.; Diez-Castellnou, M.; Perrone, B.; Rastrelli, F.; Mancin, F. Nanoparticle-Assisted NMR Detection of Organic Anions: From Chemosensing to Chromatography. *J. Am. Chem. Soc.* **2015**, *137*, 886-892.

(59) Salvia, M. V.; Salassa, G.; Rastrelli, F.; Mancin, F. Turning Supramolecular Receptors into Chemosensors by Nanoparticle-Assisted "NMR Chemosensing". *J. Am. Chem. Soc.* **2015**, *137*, 11399-11406.

(60) Riccardi, L.; Gabrielli, L.; Sun, X. H.; De Biasi, F.; Rastrelli, F.; Mancin, F.; De Vivo, M. Nanoparticle-Based Receptors Mimic Protein-Ligand Recognition. *Chem* **2017**, *3*, 92-109.

(61) Bonomi, R.; Cazzolaro, A.; Prins, L. J. Assessment of the Morphology of Mixed SAMs on Au Nanoparticles Using a Fluorescent Probe. *Chem. Commun.* **2011**, *47*, 445-447.

(62) Pieters, G.; Cazzolaro, A.; Bonomi, R.; Prins, L. J. Self-Assembly and Selective Exchange of Oligoanions on the Surface of Monolayer Protected Au Nanoparticles in Water. *Chem. Commun.* **2012**, *48*, 1916-1918.

(63) Pieters, G.; Pezzato, C.; Prins, L. J. Controlling Supramolecular Complex Formation on the Surface of a Monolayer-Protected Gold Nanoparticle in Water. *Langmuir* **2013**, *29*, 7180-7185.

(64) Maiti, S.; Pezzato, C.; Martin, S. G.; Prins, L. J. Multivalent Interactions Regulate Signal Transduction in a Self-Assembled Hg^{2+} Sensor. *J. Am. Chem. Soc.* **2014**, *136*, 11288-11291.

(65) Maiti, S.; Prins, L. J. Dynamic Combinatorial Chemistry on a Monolayer Protected Gold Nanoparticle. *Chem. Commun.* **2015**, *51*, 5714-5716.

(66) Pezzato, C.; Maiti, S.; Chen, J. L. Y.; Cazzolaro, A.; Gobbo, C.; Prins, L. J. Monolayer Protected Gold Nanoparticles with Metal-Ion Binding Sites: Functional Systems for Chemosensing Applications. *Chem. Commun.* **2015**, *51*, 9922-9931.

(67) Hill, H. D.; Millstone, J. E.; Banholzer, M. J.; Mirkin, C. A. The Role Radius of Curvature Plays in Thiolated Oligonucleotide Loading on Gold Nanoparticles. *ACS Nano* **2009**, *3*, 418-424.

(68) Browne, K. P.; Grzybowski, B. A. Controlling the Properties of Self-Assembled Monolayers by Substrate Curvature. *Langmuir* **2011**, *27*, 1246-1250.

(69) Wang, D.; Nap, R. J.; Lagzi, I.; Kowalczyk, B.; Han, S.; Grzybowski, B. A.; Szleifer, I. How and Why Nanoparticle's Curvature Regulates the Apparent pK_a of the Coating Ligands. *J. Am. Chem. Soc.* **2011**, *133*, 2192-2197.

(70) Walker, D. A.; Leitsch, E. K.; Nap, R. J.; Szleifer, I.; Grzybowski, B. A. Geometric Curvature Controls the Chemical Patchiness and Self-Assembly of Nanoparticles. *Nature Nanotech.* **2013**, *8*, 676-681.

(71) Lin, W.; Murphy, C. J. A Demonstration of Le Chatelier's Principle on the Nanoscale. *ACS Cent. Sci.* **2017**, *3*, 1096-1102.

(72) Wang, X.; Ramström, O.; Yan, M. D. Quantitative Analysis of Multivalent Ligand Presentation on Gold Glyconanoparticles and the Impact on Lectin Binding. *Anal. Chem.* **2010**, *82*, 9082-9089.

(73) Wang, X.; Matei, E.; Gronenborn, A. M.; Ramström, O.; Yan, M. D. Direct Measurement of Glyconanoparticles and Lectin Interactions by Isothermal Titration Calorimetry. *Anal. Chem.* **2012**, *84*, 4248-4252.

(74) Wang, X.; Matei, E.; Deng, L. Q.; Ramström, O.; Gronenborn, A. M.; Yan, M. D. Multivalent Glyconanoparticles with Enhanced Affinity to the Anti-Viral Lectin Cyanovirin-N. *Chem. Commun.* **2011**, *47*, 8620-8622.

(75) Chuang, Y. J.; Zhou, X. C.; Pan, Z. W.; Turchi, C. A Convenient Method for Synthesis of Glyconanoparticles for Colorimetric Measuring Carbohydrate-Protein Interactions. *Biochem. Biophys. Res. Commun.* **2009**, *389*, 22-27.

(76) Nel, A. E.; Maedler, L.; Velegol, D.; Xia, T.; Hoek, E. M. V.; Somasundaran, P.; Klaessig, F.; Castranova, V.; Thompson, M. Understanding Biophysicochemical Interactions at the Nano-Bio Interface. *Nature Mater.* **2009**, *8*, 543-557.

(77) Mu, Q. X.; Jiang, G. B.; Chen, L. X.; Zhou, H. Y.; Fourches, D.; Tropsha, A.; Yan, B. Chemical Basis of Interactions between Engineered Nanoparticles and Biological Systems. *Chem. Rev.* **2014**, *114*, 7740-7781.

(78) Templeton, A. C.; Hostetler, M. J.; Kraft, C. T.; Murray, R. W. Reactivity of Monolayer-Protected Gold Cluster Molecules: Steric Effects. *J. Am. Chem. Soc.* **1998**, *120*, 1906-1911.

(79) Zhu, J.; Ganton, M. D.; Kerr, M. A.; Workentin, M. S. Chemical Modification of Monolayer-Protected Gold Nanoparticles Using Hyperbaric Conditions. *J. Am. Chem. Soc.* **2007**, *129*, 4904-4905.

(80) Gobbo, P.; Luo, W.; Cho, S. J.; Wang, X. X.; Biesinger, M. C.; Hudson, R. H. E.; Workentin, M. S. Small Gold Nanoparticles for Interfacial Staudinger-Bertozzi Ligation. *Org. Biomol. Chem.* **2015**, *13*, 4605-4612.

(81) Luo, W.; Gobbo, P.; McNitt, C. D.; Sutton, D. A.; Popik, V. V.; Workentin, M. S. "Shine & Click" Photo-Induced Interfacial Unmasking of Strained Alkynes on Small Water-Soluble Gold Nanoparticles. *Chem. - Eur. J.* **2017**, *23*, 1052-1059.

(82) Kolmel, D. K.; Kool, E. T. Oximes and Hydrazones in Bioconjugation: Mechanism and Catalysis. *Chem. Rev.* **2017**, *117*, 10358-10376.

(83) Higgs, P. L.; Ruiz-Sanchez, A. J.; Dalmina, M.; Horrocks, B. R.; Leach, A. G.; Fulton, D. A. Enhancing the Kinetics of Hydrazone Exchange Processes: An Experimental and Computational Study. *Org. Biomol. Chem.* **2019**, *17*, 3218-3224.

(84) Posocco, P.; Gentilini, C.; Bidoggia, S.; Pace, A.; Franchi, P.; Lucarini, M.; Fermeglia, M.; Pricl, S.; Pasquato, L. Self-Organization of Mixtures of Fluorocarbon and Hydrocarbon Amphiphilic Thiolates on the Surface of Gold Nanoparticles. *ACS Nano* **2012**, *6*, 7243-7253.

(85) Şologan, M.; Marson, D.; Polizzi, S.; Pengo, P.; Boccardo, S.; Pricl, S.; Posocco, P.; Pasquato, L. Patchy and Janus Nanoparticles by Self-Organization of Mixtures of Fluorinated and Hydrogenated Alkanethiolates on the Surface of a Gold Core. *ACS Nano* **2016**, *10*, 9316-9325.

(86) Marson, D.; Guida, F.; Şologan, M.; Boccardo, S.; Pengo, P.; Perissinotto, F.; Iacuzzi, V.; Pellizzoni, E.; Polizzi, S.; Casalis, L.; Pasquato, L.; Pacor, S.; Tossi, A.; Posocco, P. Mixed Fluorinated/Hydrogenated Self-Assembled Monolayer-Protected Gold Nanoparticles: *In Silico* and *In Vitro* Behavior. *Small* **2019**, *15*, 1900323.

(87) Luo, Z.; Marson, D.; Ong, Q. K.; Loiudice, A.; Kohlbrecher, J.; Radulescu, A.; Krause-Heuer, A.; Darwish, T.; Balog, S.; Buonsanti, R.; Svergun, D. I.; Posocco, P.; Stellacci, F. Quantitative 3D Determination of Self-Assembled Structures on Nanoparticles Using Small Angle Neutron Scattering. *Nat. Commun.* **2018**, *9*, 1343.

(88) Wang, J. H.; Kenseth, J. R.; Jones, V. W.; Green, J. B. D.; McDermott, M. T.; Porter, M. D. SFM Tip-Assisted Hydrolysis of a Dithiobis(Succinimidoundecanoate) Monolayer Chemisorbed on a Au(111) Surface. *J. Am. Chem. Soc.* **1997**, *119*, 12796-12799.

(89) Shovsky, A.; Schonherr, H. New Combinatorial Approach for the Investigation of Kinetics and Temperature Dependence of Surface Reactions in Thin Organic Films. *Langmuir* **2005**, *21*, 4393-4399.

(90) Schonherr, H.; Feng, C. L.; Shovsky, A. Interfacial Reactions in Confinement: Kinetics and Temperature Dependence of Reactions in Self-Assembled Monolayers Compared to Ultrathin Polymer Films. *Langmuir* **2003**, *19*, 10843-10851.

(91) Dugas, V.; Chevalier, Y. Chemical Reactions in Dense Monolayers: *In Situ* Thermal Cleavage of Grafted Esters for Preparation of Solid Surfaces Functionalized with Carboxylic Acids. *Langmuir* **2011**, *27*, 14188-14200.

(92) Chu, Z. L.; Han, Y. X.; Bian, T.; De, S.; Král, P.; Klajn, R. Supramolecular Control of Azobenzene Switching on Nanoparticles. *J. Am. Chem. Soc.* **2019**, *141*, 1949-1960.

(93) Fu, Q.; Bao, X. H. Surface Chemistry and Catalysis Confined under Two-Dimensional Materials. *Chem. Soc. Rev.* **2017**, *46*, 1842-1874.

(94) Goronzy, D. P.; Ebrahim, M.; Rosei, F.; Arramel; Fang, Y.; De Feyter, S.; Tait, S. L.; Wang, C.; Beton, P. H.; Wee, A. T. S.; Weiss, P. S.; Perepichka, D. F. Supramolecular Assemblies on Surfaces: Nanopatterning, Functionality, and Reactivity. *ACS Nano* **2018**, *12*, 7445-7481.

(95) Grommet, A. B.; Feller, M.; Klajn, R. Chemical Reactivity under Nanoconfinement. *Nature Nanotech.* **2020**, *15*, 256-271.

(96) Brown, W. M.; Kohlmeyer, A.; Plimpton, S. J.; Tharrington, A. N. Implementing Molecular Dynamics on Hybrid High Performance Computers - Particle-Particle Particle-Mesh. *Comput. Phys. Commun.* **2012**, *183*, 449-459.

(97) Nguyen, T. D.; Plimpton, S. J. Accelerating Dissipative Particle Dynamics Simulations for Soft Matter Systems. *Comput. Mater. Sci.* **2015**, *100, Part B*, 173-180.

(98) Case, D. A.; Ben-Shalom, I. Y.; Brozell, S. R.; Cerutti, D. S.; Cheatham, T. E., III; Cruzeiro, V. W. D.; Darden, T. A.; Duke, R. E.; Ghoreishi, D.; Gilson, M. K.; Gohlke, H.; Goetz, A. W.; Greene, D.; Harris, R.; Homeyer, N.; Izadi, S.; Kovalenko, A.; Kurtzman, T.; Lee, T. S.; LeGrand, S., *et al. Amber 2018*, University of California: San Francisco., 2018.

(99) Giri, A. K.; Spohr, E. Influence of Chain Length and Branching on the Structure of Functionalized Gold Nanoparticles. *J. Phys. Chem. C* **2018**, *122*, 26739-26747.

(100) Mati, I. K.; Edwards, W.; Marson, D.; Howe, E. J.; Stinson, S.; Posocco, P.; Kay, E. R. Probing Multiscale Factors Affecting the Reactivity of Nanoparticle-Bound Molecules (dataset). Dataset. *University of St. Andrews Research Portal*, 2021. DOI: 10.17630/0c05bebb-30d0-4705-9551-7b71269a6e00.

TABLE OF CONTENTS ENTRY